UC Riverside
UC Riverside Previously Published Works

Title

On the role of predicted in vivo mitral valve interstitial cell deformation on its biosynthetic behavior.

Permalink

https://escholarship.org/uc/item/88x2q15h

Journal

Biomechanics and Modeling in Mechanobiology, 20(1)

Authors

Ayoub, Salma
Howsmon, Daniel
Lee, Chung-Hao
et al.

Publication Date

2021-02-01

DOI

10.1007/s10237-020-01373-w

Peer reviewed

On the role of predicted in vivo mitral valve interstitial cell deformation on its biosynthetic behavior

Salma Ayoub[1], **Daniel P. Howsmon**[1], **Chung-Hao Lee**[2], **Michael S. Sacks**[1]

[1]James T. Willerson Center for Cardiovascular Modeling and Simulation, Oden Institute for Computational Engineering and Sciences, Department of Biomedical Engineering, The University of Texas at Austin, Austin, USA

[2]School of Aerospace and Mechanical Engineering, The University of Oklahoma, Norman, OK 73019, USA

Abstract

Ischemic mitral regurgitation (IMR), a frequent complication of myocardial infarction, is characterized by regurgitation of blood from the left ventricle back into the left atrium. Physical interventions via surgery or less-invasive techniques are the only available therapies for IMR, with valve repair via undersized ring annuloplasty (URA) generally preferred over valve replacement. However, recurrence of IMR after URA occurs frequently and is attributed to continued remodeling of the MV and infarct region of the left ventricle. The mitral valve interstitial cells (MVICs) that maintain the tissue integrity of the MV leaflets are highly mechanosensitive, and altered loading post-URA is thought to lead to aberrant MVIC-directed tissue remodeling. Although studies have investigated aspects of mechanically directed VIC activation and remodeling potential, there remains a substantial disconnect between organ-level biomechanics and cell-level phenomena. Herein, we utilized an extant multiscale computational model of the MV that linked MVIC to organ-level MV biomechanical behaviors to simulate changes in MVIC deformation following URA. A planar biaxial bioreactor system was then used to cyclically stretch explanted MV leaflet tissue, emulating the in vivo changes in loading following URA. This simulation-directed experimental investigation revealed that post-URA deformations resulted in decreased MVIC activation and collagen mass fraction. These results are consistent with the hypothesis that URA failures post-IMR are due, in part, to reduced MVIC-mediated maintenance of the MV leaflet tissue resulting from a reduction in physical stimuli required for leaflet tissue homeostasis. Such information can inform the development of novel URA strategies with improved durability.

Keywords

Mitral valve; Mitral valve repair; Undersized ring annuloplasty; Biaxial bioreactor; Valve interstitial cells

---

✉Michael S. Sacks, mssacks@oden.utexas.edu.

Conflict of interest The authors declare no conflict of interest.

1 Introduction

The mitral valve (MV) serves as a fluidic check valve, ensuring unidirectional blood flow from the left atrium to the left ventricle (LV) over the cardiac cycle. This physiologic function is performed over 3 billion times over the human lifespan, adapting to both short-term (e.g., after exercise) and long-term (e.g., pregnancy) alterations in mechanical demands. This remarkable reliability is compromised in mitral regurgitation (MR), which occurs when the MV fails to fully close, causing retrograde flow from the left ventricle to the left atrium. MR is the most prevalent valvular heart disease in the USA with an estimated prevalence of 1.7% (Benjamin et al. 2019). Ischemic MR (IMR), a type of secondary MR, is caused by LV dysfunction following myocardial infarction (MI) with initially no alterations to the MV leaflet properties. This study focuses on IMR.

Treatments for IMR aim to restore unidirectional blood flow through surgical repair or replacement of the MV. In patients aged 40–49 years, replacement with a bioprosthetic is associated with a higher 15-year mortality compared with replacement with a mechanical valve, but this effect decreases with increasing age (Chikwe et al. 2015; Goldstone et al. 2017). Mechanical valve replacement is associated with increased bleeding and stroke risks (Chikwe et al. 2015; Goldstone et al. 2017), whereas replacement with a bioprosthetic is associated with elevated reoperation risk (Chikwe et al. 2015; Goldstone et al. 2017). On the other hand, repair procedures with undersized ring annuloplasty (URA) or more contemporary, less invasive approaches that utilize direct clipping of the leaflets are generally preferred over replacement due to the beneficial effects of preserving the native tissue. For instance, Acker et al. (2014) reported that URA without recurrent IMR resulted in superior LV volume reduction when compared with replacement. However, this LV volume reduction is abolished if MR recurs, which occurs in 32.6% and 58.8% of patients at 1 and 2 years post-URA (Acker et al. 2014; Goldstein et al. 2016). This substantial MR recurrence remains the critical factor limiting the success of URA for treating IMR.

Even though URA seeks to restore the overall physiological function of the MV, the repaired MV undergoes drastically different mechanical deformations during the cardiac cycle when compared with native MV deformations (Lee et al. 2017). In vitro studies on valve interstitial cells (VICs), the resident cells that are responsible for maintaining the structure and composition of the heart valves, have revealed that altered mechanics alone can stimulate signaling pathways associated with MV remodeling (Wang et al. 2012; Quinlan and Billiar 2012; Poggio et al. 2013; Gould et al. 2016; Ayoub et al. 2017). These in vitro studies have outlined key proteins and deformation-driven processes that contribute to VIC activation and VIC-directed remodeling, but there remains a general lack of connection to higher, clinically relevant scales. An improved understanding of the mechanically driven MV remodeling process is needed to optimize URA procedures for minimizing recurrence risk.

Computational models of heart valve function have matured greatly in recent years (Votta et al. 2008; Wang and Sun 2013; Sturla et al. 2017; Sacks et al. 2019). However, existing computational models have yet to account for all of the underlying features that impact long-term MV behavior. In addition to altered loading, growth and remodeling in the

MV following MI and after surgery undoubtedly also play a major role in determining the success or failure of URA (Rego et al. 2017). Recent work has uncovered evidence of significant cell activation and extracellular matrix (ECM) turnover in the MV leaflets following MI (Dal-Bianco et al. 2009). This has been underscored by recent animal post-MI studies conducted by Rego rt al. (2017), where analysis of resultant rt-3DE images demonstrated that the MV annulus was substantially dilated and flattened post-MI. MI-induced effects propagated throughout both leaflets to yield substantial changes in strain patterns, including a pronounced increase in leaflet dimensions. Despite its importance, the mechanism through which the MV remodels in response to MI—as well as what mediates this process—remains poorly understood. In addition to immediate post-surgical applications, high-fidelity computer simulations provide a means to connect cellular function with organ-level MV tissue mechanical responses and to aid the design of optimal MV URA strategies. However, extending these models to cellular and subcellular scales that describe fundamental VIC-driven remodeling processes require a detailed understanding of the relationship between MVIC deformation and pre- and post-URA MV leaflet deformation.

The choice of reference configuration is a key consideration in the development of computational models that bridge in vitro and in vivo studies. Chuong and Fung (1986) and Fung (1991) have gained important insights in this regard by considering "residual stresses" or "pre-stresses." Amini et al. (2012) demonstrated the presence of substantial MV pre-strains, and Lee et al. (2017) illustrated the functional implications of this pre-strain that impact how material models based on in vitro experiments need to be used for in-vivo stress prediction. When attempting to connect to in vivo MVIC mechanobiological responses, reference configurations provide crucial information on the homeostatic tissue deformation in the MV and need to be incorporated into any in vitro study attempting to replicate the in vivo condition.

The MVIC nuclear aspect ratio (NAR) has been shown to be a key metric of cell deformation for monitoring VIC activation and VIC-derived remodeling. Nuclear deformation regulates a variety of cellular processes, including cell migration (Salvermoser et al. 2018; Krause and Wolf 2015), cell cycle progression (Aureille et al. 2019), and cancer cell malignancy (Antmen et al. 2019). Nuclear deformation is directly involved in YAP-dependent mechanotransduction by altering transport across nuclear pores (Elosegui-Artola et al. 2017). In VICs, the NAR is correlated with collagen production, cell proliferation, and alpha-smooth muscle actin (a-SMA) expression (Lam et al. 2016; Ayoub et al. 2017). Thus, the NAR is a useful metric for evaluating the overall VIC biosynthetic state. However, a quantitative link between alterations in the organ-level functional state and the cellular mechanobiology has yet to be firmly established.

In an earlier study, Ayoub et al. (2017) utilized a simple tissue strip approach to elucidate MV anterior leaflet tissue and MVIC responses to varying tissue strain levels. Comprehensive results at different length scales revealed that normal responses are observed only within a defined range of tissue deformations, whereas deformations outside of this range lead to hypo- and hyper-synthetic responses, evidenced by changes in a-SMA, type I collagen, and other ECM and cell adhesion molecule regulation (Ayoub et al. 2017).

Furthermore, Ayoub et al. (2017) identified MVIC deformation as a key player in leaflet tissue homeostatic regulation and, as such, used it as the metric that makes the critical link between in vitro responses and simulated equivalent in vivo behavior. Results indicated that MVIC responses have a delimited range of in vivo deformations that maintain a homeostatic response, suggesting that deviations from this range may lead to deleterious tissue remodeling and failure. In a subsequent study, Lee et al. (2017) incorporated in vivo MV anterior leaflet (MVAL) deformations and pre-strains into an inverse finite element (FE) modeling framework to estimate the resulting in vivo tissue pre-stresses peak functional stresses. By integrating the tissue-level kinematic results into a downscale MVIC microenvironment FE model, we were able to estimate (for the first time) the in vivo *layer-specific* MVIC deformations and deformation rates of normal and surgically repaired MVALs. From these simulations, Lee et al. (2017) determined that URA greatly reduced peak MVIC deformation levels in a layer-specific manner. This suggests that the associated reductions in MVIC deformation may down-regulate MV ECM maintenance, ultimately leading to reduction in tissue mechanical integrity.

Collectively, these studies have provided valuable insight into MVIC mechanobiology in response to organ/tissue-level alternations induced by MV disease or URA. However, further attempts to refine such approaches must be built on more complete information on the interplay between organ-/tissue-level kinematics and MVIC deformations and the resulting deviations from homeostatic biosynthetic responses. Given the complexity of MV leaflet deformations (Lee et al. 2017; Rego et al. 2018) and complex coupling to MVIC deformations (Ayoub et al. 2017, 2018), such studies must involve more realistic in vitro tissue kinematics that attempt to mimic the actual in vivo environment. Toward this end, the present study utilized a biaxial deformation–based experimental methodology to better explore the relation between MVIC mechanobiology and alterations in the in vivo deformation due to URA. Using a simulation-informed approach, novel experiments were performed that sought to mimic the effects of URA on the MV and account for MV pre-strain. Coupling these in vivo-mimicking cyclic biaxial mechanical tests with a panel of assays to determine key ECM biosynthetic responses and VIC activation levels, this study makes a crucial link between altered VIC deformation and altered VIC-driven remodeling.

2 Methods

2.1 Overall approach

The key hypothesis in the present study is that cyclic strain amplitude of the MVIC over the cardiac cycle, as quantified by the NAR, is a key determinant of MVIC mechanobiological response. Using an FE modeling approach based on in vivo deformations (Fig. 1), Lee et al. (2017) have previously shown that URA not only greatly reduces the MV leaflet circumferential strain during closure (without detectably changing the radial strains), but also reduced the peak MVIC NAR.

To assess this hypothesis in the context of alterations in MVIC deformations in URA, we implemented deformations derived from computational biomechanics simulations in a custom planar biaxial bioreactor system (PBBS) to assess short-term (48 h) MVIC mechanobiological responses to the altered MVAL cyclic stretch levels that emulate URA. A

key aspect of this approach is the use of a multiscale-MVAL model that incorporates leaflet pre-strain to derive conditions mimicking the in vivo conditions (Ayoub et al. 2017; Lee et al. 2017). This in vitro experimental approach, driven by in vivo–informed simulations, allowed us to approximate changes in both tissue-level deformation and MVIC NAR in order to evaluate key mechanobiological responses.

2.2 Simulation-designed experimental protocols

2.2.1 Reference configurations from Lee et al. (2017)—A fundamental question underlying this work revolves around the importance of reproducing the in vivo reference configuration. Based on results from Lee et al. (2017), the following kinematic states were utilized (Fig. 1c):

1. β_0: The in vitro unloaded configuration.

2. β_1: The immediately exised, unloaded state after the MV was excised from the heart. This is not equivalent to β_0 due to tissue relaxation, ceasing ~24 h after excision.

3. β_2: The in vivo reference configuration associated with the onset of ventricular contraction (OVC) (Fig. 1b).

4. β_t^{Normal} and β_t^{Ring}: The loaded states for any time t.

As seen in Figs. 1c and 2, the choice of reference configuration has substantial effects on the resulting deformation.

2.2.2 Simulation-derived stresses and deformations—Herein, we used in vivo simulations from Lee et al. (2017) to determine the operational pre-stress, normal peak stress, and URA peak stress used in the in vitro experimental platform developed in this work. Lee et al. (2017) estimated MVAL stresses using an inverse FE modeling framework, based on in vivo measures of tissue deformations (Figs. 1 and 3). Briefly, MV in vivo tissue-level kinematic data were integrated into a downscale MVIC microenvironment FE model, enabling the estimation of in vivo layer-specific MVIC deformations and deformation rates of normal and surgically repaired MVALs. Using this same approach, we estimated the in vivo loading conditions in our in vitro system (see Sect. 2.3) necessary to estimate the equivalent in vivo MV tissue first Piola–Kirchhoff stress ($\mathbf{P}$) levels for the pre-stress state, as well as the normal peak stress (end systolic) state. Due to differences in tissue samples [juvenile sheep here compared with the adult sheep used in Lee et al. (2017)] and the increased stress at the boundary of the cruciate samples (Sun et al. 2005), the normal peak stress was reduced by 10%; however, this normal peak stress is in the fully loaded regime and this slight modification has negligible impact on the resulting deformation. For the ring peak stress state, P_{RR} was fixed to that of the normal peak stress state and P_{CC} was calibrated to achieve the computationally predicted drop in NAR (Fig. 3c). With an estimated NAR reduction of one-third, a P_{CC} of 82.0 kPa was selected to represent the peak URA state. Figure 4c also indicates that at P_{RR} = 387.2 kPa and P_{CC} = 200 kPa, the deformation results in an average NAR of 5.95, which is already very close to the NAR of

6.02 at P_{RR} = 387.2 kPa and P_{CC} = 320.9 kPa, indicating the normal peak stress is well within the fully loaded regime.

2.3 Experimental procedures

Using the operational stresses determined from Sect. 2.2.2, the following experiments were conducted in this work.

2.3.1 Planar biaxial bioreactor system (PBBS)—

We developed a tissue culture system specialized for valve leaflet tissues capable of imposing controlled planar biaxial loading to replicate physiological in vivo strains. In brief, the design consisted of four linear actuators and two load cells, one on each axis (Fig. 4a). A four-pillared stacking system in the middle of the system holds the specimen chamber, which is made of wear-resistant and temperature-stable polysulfone. A clamp tissue attachment system is used to mount the tissue inside the specimen chambers. The system can operate in either strain- or stress-controlled modes, with each axis having a different limit. Due to the inherent difficulties of tracking strains while the samples are in the incubator, the PBBS was operated in the stress-controlled mode in this study. Local tissue strain was determined by tracking four fiducial markers on the specimen surface using standard methods to compute the 2D deformation gradient tensor **F**. We note that $\lambda_1 = \lambda_c = F_{11}$, $\lambda_2 = \lambda_R = F_{22}$ and shearing deformation components $F_{12} \approx 0$ and $F_{21} \approx 0$. All components that are housed within the specimen chamber are sterilized via autoclave and ultraviolet exposure.

2.3.2 Tissue preparation and experimental protocol—

Fresh ovine hearts were collected from 6–10 month lambs from a local USDA approved abattoir (Mercantile Meat Processing Company, Utopia, TX) within 30 min of slaughter. MVALs were isolated on site and submerged in ice-cold Hypothermosol FRS (Sigma-Aldrich, St. Louis, MO) for transport to the laboratory. Once in the laboratory, cruciform shaped samples (5–7 mm × 3–4 mm, circumferential × radial) were dissected from the upper central region wherein chordae tendonae attachments did not occur and mounted onto the PBBS. Unloaded, postmortem control samples were acquired using the same approach; then, snap frozen with liquid nitrogen and stored at –80°C. These unloaded control samples were not loaded in the bioreactor.

For NAR evaluation, samples were statically stretched and fixed under either (1) unloaded, postmortem control, (2) pre-stress, or (3) normal peak stress. Additional samples were used for calibrating the URA peak stress. For ECM and αSMA, samples were either (1) unloaded, postmortem control, (2) cycled between pre-stress and normal peak stress, or (3) cycled between pre-stress and URA peak stress. For each treatment group, $n = 3$ MVAL specimens were used. Samples were mounted in the bioreactor specimen chamber aseptically in a sterile laminar flow hood. Each specimen chamber was filled with 12 mL of serum-free DMEM (Life Technologies, Carlsbad, CA) supplemented with 1% (v/v) Pen/Strep antibiotics (Invitrogen, Carlsbad, CA), 1% (v/v) L-glutamine (Bio-Whittaker, Houston, TX), 10% (v/v) fetal bovine serum (Hyclone, Logan, UT), and 0.4% (v/v) fungizone (Invitrogen, Carlsbad, CA). The specimen chamber was then attached to the system base of each modular bioreactor, which is housed within the incubator maintained at 37°C and

5% CO_2. Samples undergoing cyclic deformation were then stretched for a total of 48 h. At the end of each treatment, samples were either fixed or snap-frozen for further analysis as described. Assessment of the average NAR in the unloaded configurations after 48 h cyclic stretch from pre-stress to normal peak stress (3.54 ± 0.19) or URA peak stress (2.83 ± 0.82) compared with postmortem controls (2.86 ± 0.30) indicates that minimal permanent set occurs.

2.3.3 Cell deformation—In a separate group of experiments, three MVALs were used for microenvironment and cell deformation analysis. Similarly, MVALs were isolated and stored in hypothermosol. Cruciform shaped samples were dissected from the clear zone and mounted onto the biaxial bioreactor specimen chamber. Tissue dimensions (circumferential and radial lengths and average thickness across three points in the middle) are input into the control software GUI. The individual wells of the specimen chamber were filled with PBS and the specimen placed in each well as described above. Each group of $n = 3$ samples was subjected to a single stress level: pre-stress, normal peak stress, or URA peak stress (Fig. 4).

2.3.4 Histology and immunohistochemistry—Tissue preparation for histology and immunohistochemistry has been described previously (Balachandran et al. 2006; Merryman et al. 2007). Briefly, MVAL samples (both control and treated) were fixed with 10% buffered formalin (or EM grade glutaraldehyde for the fixation studies), transferred to 70% ethanol for storage, embedded in paraffin, cut into 5-μm sections, and mounted on glass slides. Slides were then stained with Movat's Pentachrome for layer dimensional analysis and hematoxylin and eosin (H&E) to assess cell density. Slides were imaged using a light microscope at 4× magnification (Leica, Wetzlar, Germany). MVIC NAR was also quantified after 48 h of cyclic stretch. In brief, images of the H&E-stained slides were processed in ImageJ. The average fibrosa NAR was measured for $n = 3$ samples per group by detecting all of the dark purple nuclei in the image, randomly selecting 10 nuclei/sample, and determining their best-fit ellipses. The NAR is then calculated from the average ratio of the major and minor axes of the best-fit ellipse. Immunohistochemistry was performed to determine valve interstitial cell phenotypic activation using the myofibroblast marker, aSMA. In brief, slides were deparaffinized, hydrated, and incubated in 10% goat serum and 0.03% hydrogen peroxide for 15 min each. The primary rabbit polyclonal a-SMA antibody (1:100, Abcam, Cambridge, MA) was applied for 40 min followed by the anti-rabbit peroxidase-labeled polymer for 30 min. Slides were then rinsed in PBS containing 0.01% Tween-20 after each incubation/staining step. All slides were counterstained with Mayer's hematoxylin (Dako, Carpenteria, CA), dehydrated, and mounted.

2.3.5 Protein synthesis—Acid-pepsin soluble collagen, sulfated GAG (s-GAG), and elastin content were quantified using the Sircol, Blyscan, and Fastin quantitative dye-binding assay kits, respectively (Biocolor, Belfast, UK). Samples were weighed before and after lyophilization (wet weight and dry weight, respectively). Samples were digested in 1% (w/v) pepsin in 0.5M acetic acid (Sigma-Aldrich, St. Louis, MO) for 24 h at 4°C for collagen quantification, 1% papain (Sigma-Aldrich, St. Louis, MO) for 15 h at 60°C for s-GAG content, and in 0.25M of oxalic acid at 100°C for 1 h for elastin assessment. Digests were then quantified using manufacturers' protocols.

2.3.6 Statistical analysis—Colorimetric assay values (collagen, s-GAG, and elastin) and NARs are reported as mean ± standard error. For statistical comparison, colorimetric values were analyzed with a one-tailed Student's *t* test. NAR was analyzed with a two-tailed Student's *t* test. All statistical analyses were performed in MATLAB (MathWorks, Natick, MA).

3 Results

3.1 Bioreactor assessment: actuator displacement and strain measurement

To assess the bioreactor function and actuator displacement, we measured the clamp-to-clamp stretch for the following groups: (1) unloaded to pre-stress, (2) pre-stress to normal peak stress, and (3) pre-stress to URA peak stress. Similarly, we used fiducial marker data to compute the deformation gradient for each of these groups. The circumferential and radial right stretches for the normal stress group are $4.1 \pm 7.2\%$ and $10.9 \pm 5.4\%$, respectively.

3.2 Mitral valve interstitial cell deformation under normal stress

H&E images were used to quantify the MIVC NAR in the control, pre-stress, and normal states (Fig. 5). As in previous studies, the NAR increases with increasing stress. The difference between the NAR values in the control, pre-stress, and normal samples is statistically significant across all three groups ($p < 0.01$). Whereas this may be expected between the normal peak stress and the other groups, the significant difference between the pre-stress and unloaded control groups highlight the importance of incorporating pre-stress into both computational models and in vitro experimental platforms for investigating valve biomechanics.

3.3 Biosynthetic response: homeostasis and ring repair

Various studies have investigated VIC responses to mechanical stimuli, including more recent ones carried out by our own group (Ayoub et al. 2016, 2017). Results follow a trend: phenotypic activation, increased synthesis of PGs, GAGs (Gupta and Grandeallen 2006; Gupta et al. 2009; Lacerda et al. 2012) and collagen (Balachandran et al. 2006; Merryman et al. 2007), as well as increased proteolytic expression and activity (Balachandran et al. 2006, 2009). The mass fractions of acid-pepsin-soluble collagen and s-GAGs are decreased in the ring stress group compared with the normal stress group, whereas elastin levels remain unchanged (Fig. 6a–c), consistent with previous reports.

3.4 MVIC activation after URA stress treatment

VICs are typically fibroblast-like, but become activated to a myofibroblast phenotype in development and disease (Rabkin et al. 2001). Phenotypic activation is typically characterized by an upregulation of a-SMA (Taylor et al. 2003), whereby MVICs become myofibroblasts and begin to actively remodel the ECM, highlighting the fact that VIC phenotypic state is linked to the remodeling demands of the tissue (Rabkin et al. 2002). Herein, VIC phenotypic activation was significantly reduced after cycling from pre-stress to URA peak stress compared with cycling from pre-stress to normal peak stress (2.28 ± 0.83 vs. 4.80 ± 0.42, $p < 0.05$).

4 Discussion

4.1 Approach

In the present study, we utilized the simulation methodology of Lee et al. (2017) to predict in vivo post-surgical repair MVIC deformations to design the in vitro experiments carried out in this work. Developing an in vitro system that emulated in vivo deformations was crucially dependent on computational simulations of MVAL and MVIC biomechanics. We were able to recapitulate the in vivo functional state in the in vitro PBBS, as well as incorporate pre-stresses into the experimental reference configuration to allow for more faithful representation of the in vivo tissue deformations.

The present study builds upon Ayoub et al. (2017), wherein MVIC deformation was identified as a key metric in predicting VIC activation and ECM regulation. However, the in vitro experimental "strip biaxial" system was not able to fully reproduce in vivo tissue-level deformation modes, which we have shown in the past to be multiaxial (Sacks et al. 2006). Prior work on the role of mechanical stimuli on MVAL tissue and their resident MVICs have relied solely on in vitro and ex vivo techniques that were only able to roughly approximate the in vivo environment (Ayoub et al. 2017; Balachandran et al. 2006, 2009; Lacerda et al. 2012; Lam et al. 2016; Merryman et al. 2007; Sacks et al. 2009; Thayer et al. 2011). By more faithfully capturing the MVICs' in vivo mechanical environment, we were able to demonstrate closer equivalence to the in vivo environment and measure key MVIC responses that would be expected to occur in vivo.

4.2 Changes in MV leaflet ECM mass fractions can be predicted from MVIC NAR

Despite species differences between the porcine samples used by Ayoub et al. (2017) and the ovine samples used herein, the relationships between MVIC NAR and ECM mass fractions were surprisingly consistent (Fig. 7 and Table 1). A study by Lam et al. (2016) that artificially confined single VICs in specified geometries also indicates that decreasing NAR leads to decreased VIC contractility and a-SMA expression. In synthetic hydrogel systems, Mabry et al. (2016) have shown that culturing VICs in a 3D environment better reproduces the in vivo VIC phenotype over culturing on 2D substrates. Thus, we believe the most interesting finding of the present study was the underscoring of the pivotal role of MVIC deformation in modulating their phenotypic and biosynthetic responses. Moreover, the PBBS system developed herein can be used as an in vitro platform to test the effects of biochemical stimuli and potential pharmaceutical treatments to the physiological function of the MV.

4.3 Limitations

While this study made substantial strides in mimicking the in vivo mechanical environment in an in vitro system, limitations remain. The clamps used to attach the tissue and the cruciate shape of the specimens are known to produce nonuniform stress and strain fields (Sun et al. 2005). However, the small size of the specimens and the 48-h duration of the experiment dictated such an experimental system setup. Yet, the close agreement in NAR in our studies (Fig. 7) suggests that the current approach provided a good approximation. Other, likely secondary factors such as shear forces from blood flow were not incorporated

in the in vitro system. These effects have been incorporated into previous flex-stretch-flow bioreactor systems (Engelmayr et al. 2008); however, such devices only incorporate basic aspects of each kind of mechanical force and not the precise control that facilitates in vivo emulation afforded by the PBBS system used in this study. Our knowledge of how valvular endothelium signal to the VIC population in the functioning valve remains very limited, and much more work is required to elucidate these effects.

While we have connected MV deformations with macro, tissue-level production of key structural proteins, the underlying mechanotransduction mechanisms and how they interact with other signaling mechanisms brought on by IMR and MV repair remain poorly understood. Connecting down to models of relevant signaling mechanisms provides a promising avenue for understanding the role of VIC mechanobiology in healthy and diseased environments and developing pharmaceutical interventions to aid or replace current surgical therapies.

5 Conclusions and future directions

Computational models of physiological systems provide useful avenues for connecting the various spatial and temporal scales that are responsible for biological complexity. Furthermore, the expense and ethics of large-scale in vivo experiments, especially large animal models of disease, necessitate in vitro systems for detailed experimental analyses. Using simulations of in vivo MV deformations to drive in vitro experiments on MVIC deformations and their subsequent remodeling response, this study replicated several key aspects of the in vivo environment in an in vitro emulating environment. Our results were consistent with the hypothesis that URA failures post-IMR are due, in part, to reduced MVIC-mediated maintenance of the MV leaflet tissue resulting from a reduction in physical stimuli required for leaflet tissue homeostasis.

The results from this paper are thus not restricted to a specific URA procedure. The basis for this is that all URA techniques decrease peak circumferential stress while leaving the peak radial stress relatively unchanged. This is because all URA designs/procedures seek to substantially reduce the MV annular size to enable proper coaptation and functional restoration. Thus, the exact change in the valve-level stress profile and the change in average NAR will be dependent on the annuloplasty ring type (and more importantly on the patient-specific MV geometry), but the general trend will be the same regardless of annuloplasty ring selection. Such information can inform the development of novel MV surgical repair strategies with improved durability.

References

Acker MA, Parides MK, Perrault LP, Moskowitz AJ, Gelijns AC, Voisine P, Smith PK, Hung JW, Blackstone EH, Puskas JD (2014) Mitral-valve repair versus replacement for severe ischemic mitral regurgitation. N Engl J Med 370(1):23–32. 10.1056/NEJMoa1312808 [PubMed: 24245543]

Amini R, Eckert CE, Koomalsingh K, McGarvey J, Minakawa M, Gorman JH, Gorman RC, Sacks MS (2012) On the in vivo deformation of the mitral valve anterior leaflet: effects of annular geometry and referential configuration. Ann Biomed Eng 40(7):1455–1467. 10.1007/s10439-012-0524-5 [PubMed: 22327292]

Antmen E, Demirci U, Hasirci V (2019) Amplification of nuclear deformation of breast cancer cells by seeding on micropatterned surfaces to better distinguish their malignancies. Colloids Surf B 183:110402. 10.1016/j.colsurfb.2019.110402

Aureille J, Buffière-Ribot V, Harvey BE, Boyault C, Pernet L, Andersen T, Bacola G, Balland M, Fraboulet S, Van Landeghem L, Guilluy C (2019) Nuclear envelope deformation controls cell cycle progression in response to mechanical force. EMBO Rep 20(9). 10.15252/embr.201948084

Ayoub S, Ferrari G, Gorman RC, Gorman JH, Schoen FJ, Sacks MS (2016) Heart valve biomechanics and underlying mechanobiology. In: Terjung R (ed) Comprehensive physiology. Wiley, Hoboken, pp 1743–1780. 10.1002/cphy.c150048

Ayoub S, Lee CH, Driesbaugh KH, Anselmo W, Hughes CT, Ferrari G, Gorman RC, Gorman JH, Sacks MS (2017) Regulation of valve interstitial cell homeostasis by mechanical deformation: implications for heart valve disease and surgical repair. J R Soc Interface 14(135):20170580. 10.1098/rsif.2017.0580

Ayoub S, Tsai KC, Khalighi AH, Sacks MS (2018) The three-dimensional microenvironment of the mitral valve: insights into the effects of physiological loads. Cell Mol Bioeng 11(4):291–306. 10.1007/s12195-018-0529-8 [PubMed: 31719888]

Balachandran K, Konduri S, Sucosky P, Jo H, Yoganathan AP (2006) An ex vivo study of the biological properties of porcine aortic valves in response to circumferential cyclic stretch. Ann Biomed Eng 34(11):1655–1665. 10.1007/s10439-006-9167-8

Balachandran K, Sucosky P, Jo H, Yoganathan AP (2009) Elevated cyclic stretch alters matrix remodeling in aortic valve cusps: implications for degenerative aortic valve disease. Am J Physiol Heart Circ Physiol 296(3):H756–H764. 10.1152/ajpheart.00900.2008 [PubMed: 19151254]

Benjamin EJ, Muntner P, Alonso A, Bittencourt MS, Callaway CW, Carson AP, Chamberlain AM, Chang AR, Cheng S, Das SR, Delling FN, Djousse L, Elkind MS, Ferguson JF, Fornage M, Jordan LC, Khan SS, Kissela BM, Knutson KL, Kwan TW, Lackland DT, Lewis TT, Lichtman JH, Longenecker CT, Loop MS, Lutsey PL, Martin SS, Matsushita K, Moran AE, Mussolino ME, O'Flaherty M, Pandey A, Perak AM, Rosamond WD, Roth GA, Sampson UK, Satou GM, Schroeder EB, Shah SH, Spartano NL, Stokes A, Tirschwell DL, Tsao CW, Turakhia MP, VanWagner LB, Wilkins JT, Wong SS, Virani SS (2019) Heart disease and stroke statistics—2019 update: a report from the American Heart Association. Circulation 139(10):e56–e528. 10.1161/CIR.0000000000000659 [PubMed: 30700139]

Chikwe J, Chiang YP, Egorova NN, Itagaki S, Adams DH (2015) Survival and outcomes following bioprosthetic vs mechanical mitral valve replacement in patients aged 50 to 69 years. J Am Med Assoc 313(14):1435–1442. 10.1001/jama.2015.3164

Chuong CJ, Fung YC (1986) On residual stresses in arteries. J Biomech Eng 108(2):189–192. 10.1115/1.3138600 [PubMed: 3079517]

Dal-Bianco JP, Aikawa E, Bischoff J, Guerrero JL, Handschumacher MD, Sullivan S, Johnson B, Titus JS, Iwamoto Y, Wylie-Sears J, Levine RA, Carpentier A (2009) Active adaptation of the tethered mitral valve: Insights into a compensatory mechanism for functional mitral regurgitation. Circulation 120(4):334–342. 10.1161/CIRCULATIONAHA.108.846782 [PubMed: 19597052]

Elosegui-Artola A, Andreu I, Beedle AE, Lezamiz A, Uroz M, Kosmalska AJ, Oria R, Kechagia JZ, Rico-Lastres P, Le Roux AL, Shanahan CM, Trepat X, Navajas D, Garcia-Manyes S, Roca-

Cusachs P (2017) Force triggers YAP nuclear entry by regulating transport across nuclear pores. Cell 171(6):1397–1410.e14. 10.1016/j.cell.2017.10.008 [PubMed: 29107331]

Engelmayr GC Jr, Soletti L, Vigmostad SC, Budilarto SG, Federspiel WJ, Chandran KB, Vorp DA, Sacks MS (2008) A novel flex-stretch-flow bioreactor for the study of engineered heart valve tissue mechanobiology. Ann Biomed Eng 36:700–712. 10.1007/s10439-008-9447-6 [PubMed: 18253834]

Fung YC (1991) What are the residual stresses doing in our blood vessels? Ann Biomed Eng 19(3):237–249. 10.1007/BF02584301 [PubMed: 1928868]

Goldstein D, Moskowitz AJ, Gelijns AC, Ailawadi G, Parides MK, Perrault LP, Hung JW, Voisine P, Dagenais F, Gillinov AM, Thourani V, Argenziano M, Gammie JS, Mack M, Demers P, Atluri P, Rose EA, O'Sullivan K, Williams DL, Bagiella E, Michler RE, Weisel RD, Miller MA, Geller NL, Taddei-Peters WC, Smith PK, Moquete E, Overbey JR, Kron IL, O'Gara PT, Acker MA (2016) Two-year outcomes of surgical treatment of severe ischemic mitral regurgitation. N Engl J Med 374(4):344–353. 10.1056/NEJMoa1512913 [PubMed: 26550689]

Goldstone AB, Chiu P, Baiocchi M, Lingala B, Patrick WL, Fischbein MP, Woo YJ (2017) Mechanical or biologic prostheses for aortic-valve and mitral-valve replacement. N Engl J Med 377(19):1847–1857. 10.1056/NEJMoa1613792 [PubMed: 29117490]

Gould RA, Yalcin HC, MacKay JL, Sauls K, Norris R, Kumar S, Butcher JT (2016) Cyclic mechanical loading is essential for Rac1-mediated elongation and remodeling of the embryonic mitral valve. Curr Biol 26(1):27–37. 10.1016/j.cub.2015.11.033 [PubMed: 26725196]

Gupta V, Grandeallen K (2006) Effects of static and cyclic loading in regulating extracellular matrix synthesis by cardiovascular cells. Cardiovasc Res 72(3):375–383. 10.1016/j.cardiores.2006.08.017 [PubMed: 17010955]

Gupta V, Tseng H, Lawrence BD, Jane Grande-Allen K (2009) Effect of cyclic mechanical strain on glycosaminoglycan and proteoglycan synthesis by heart valve cells. Acta Biomater 5(2):531–540. 10.1016/j.actbio.2008.10.009 [PubMed: 19004676]

Krause M, Wolf K (2015) Cancer cell migration in 3D tissue: negotiating space by proteolysis and nuclear deformability. Cell Adhes Migr 9(5):357–366. 10.1080/19336918.2015.1061173

Lacerda CMR, Kisiday J, Johnson B, Orton EC (2012) Local serotonin mediates cyclic strain-induced phenotype transformation, matrix degradation, and glycosaminoglycan synthesis in cultured sheep mitral valves. Am J Physiol Heart Circ Physiol 302(10):H1983–H1990. 10.1152/ajpheart.00987.2011 [PubMed: 22345569]

Lam NT, Muldoon TJ, Quinn KP, Rajaram N, Balachandran K (2016) Valve interstitial cell contractile strength and metabolic state are dependent on its shape. Integr Biol 8(10):1079–1089. 10.1039/c6ib00120c

Lee CH, Zhang W, Feaver K, Gorman RC, Gorman JH, Sacks MS (2017) On the in vivo function of the mitral heart valve leaflet: insights into tissue-interstitial cell biomechanical coupling. Biomech Model Mechanobiol 16(5):1613–1632. 10.1007/s10237-017-0908-4 [PubMed: 28429161]

Mabry KM, Payne SZ, Anseth KS (2016) Microarray analyses to quantify advantages of 2D and 3D hydrogel culture systems in maintaining the native valvular interstitial cell phenotype. Biomaterials 74:31–41. 10.1016/j.biomaterials.2015.09.035 [PubMed: 26433490]

Merryman WD, Lukoff HD, Long RA, Engelmayr GC, Hopkins RA, Sacks MS (2007) Synergistic effects of cyclic tension and transforming growth factor-β1 on the aortic valve myofibroblast. Cardiovascular Pathology 16(5):268–276. 10.1016/j.carpath.2007.03.006 [PubMed: 17868877]

Poggio P, Sainger R, Branchetti E, Grau JB, Lai EK, Gorman RC, Sacks MS, Parolari A, Bavaria JE, Ferrari G (2013) Noggin attenuates the osteogenic activation of human valve interstitial cells in aortic valve sclerosis. Cardiovasc Res 98(3):402–410. 10.1093/cvr/cvt055 [PubMed: 23483047]

Quinlan AMT, Billiar KL (2012) Investigating the role of substrate stiffness in the persistence of valvular interstitial cell activation. J Biomed Mater Res Part A 100A(9):2474–2482. 10.1002/jbm.a.34162

Rabkin E, Aikawa M, Stone JR, Fukumoto Y, Libby P, Schoen FJ (2001) Activated interstitial myofibroblasts express catabolic enzymes and mediate matrix remodeling in myxomatous heart valves. Circulation 104(21):2525–2532. 10.1161/hc4601.099489 [PubMed: 11714645]

Rabkin E, Hoerstrup SP, Aikawa M, Mayer JE, Schoen FJ (2002) Evolution of cell phenotype and extracellular matrix in tissue-engineered heart valves during in-vitro maturation and in-vivo remodeling. J Heart Valve Dis 11(3):308–314 [PubMed: 12056720]

Rego BV, Ayoub S, Khalighi AH, Drach A, Gorman JH III, Gorman RC, Sacks MS (2017) Alterations in mechanical properties and in vivo geometry of the mitral valve following myocardial infarction. Tucson, AZ

Rego BV, Khalighi AH, Drach A, Lai EK, Pouch AM, Gorman RC, Gorman JH, Sacks MS (2018) A noninvasive method for the determination of in vivo mitral valve leaflet strains. Int J Numer Methods Biomed Eng 34(12):e3142. 10.1002/cnm.3142

Sacks MS, Enomoto Y, Graybill JR, Merryman WD, Zeeshan A, Yoganathan AP, Levy RJ, Gorman RC, Gorman JH (2006) In-vivo dynamic deformation of the mitral valve anterior leaflet. Ann Thorac Surg 82(4):1369–1377. 10.1016/j.athoracsur.2006.03.117 [PubMed: 16996935]

Sacks MS, David Merryman W, Schmidt DE (2009) On the biomechanics of heart valve function. J Biomech 42(12):1804–1824. 10.1016/j.jbiomech.2009.05.015 [PubMed: 19540499]

Sacks MS, Drach A, Lee CH, Khalighi AH, Rego BV, Zhang W, Ayoub S, Yoganathan AP, Gorman RC, Joseph HG (2019) On the simulation of mitral valve function in health, disease, and treatment. J Biomech Eng 141(7):070804. 10.1115/1.4043552

Salvermoser M, Begandt D, Alon R, Walzog B (2018) Nuclear deformation during neutrophil migration at sites of inflammation. Front Immunol 9:2680. 10.3389/fimmu.2018.02680 [PubMed: 30505310]

Sturla F, Onorati F, Puppini G, Pappalardo OA, Selmi M, Votta E, Faggian G, Redaelli A (2017) Dynamic and quantitative evaluation of degenerative mitral valve disease: a dedicated framework based on cardiac magnetic resonance imaging. J Thorac Dis 9(4):S225–S238. 10.21037/jtd.2017.03.84 [PubMed: 28540065]

Sun W, Sacks MS, Scott MJ (2005) Effects of boundary conditions on the estimation of the planar biaxial mechanical properties of soft tissues. J Biomech Eng 127(4):709–715. 10.1115/1.1933931 [PubMed: 16121542]

Taylor PM, Batten P, Brand NJ, Thomas PS, Yacoub MH (2003) The cardiac valve interstitial cell. Int J Biochem Cell Biol 35(2):113–118. 10.1016/S1357-2725(02)00100-0 [PubMed: 12479860]

Thayer P, Balachandran K, Rathan S, Yap CH, Arjunon S, Jo H, Yoganathan AP (2011) The effects of combined cyclic stretch and pressure on the aortic valve interstitial cell phenotype. Ann Biomed Eng 39(6):1654–1667. 10.1007/s10439-011-0273-x [PubMed: 21347552]

Votta E, Caiani E, Veronesi F, Soncini M, Montevecchi FM, Redaelli A (2008) Mitral valve finite-element modelling from ultrasound data: a pilot study for a new approach to understand mitral function and clinical scenarios. Philos Trans R Soc A: Math Phys Eng Sci 366(1879):3411–3434. 10.1098/rsta.2008.0095

Wang Q, Sun W (2013) Finite element modeling of mitral valve dynamic deformation using patient-specific multi-slices computed tomography scans. Ann Biomed Eng 41:142–153. 10.1007/s10439-012-0620-6 [PubMed: 22805982]

Wang H, Haeger SM, Kloxin AM, Leinwand LA, Anseth KS (2012) Redirecting valvular myofibroblasts into dormant fibroblasts through light-mediated reduction in substrate modulus. PLoS ONE 7(7):e39969. 10.1371/journal.pone.0039969 [PubMed: 22808079]
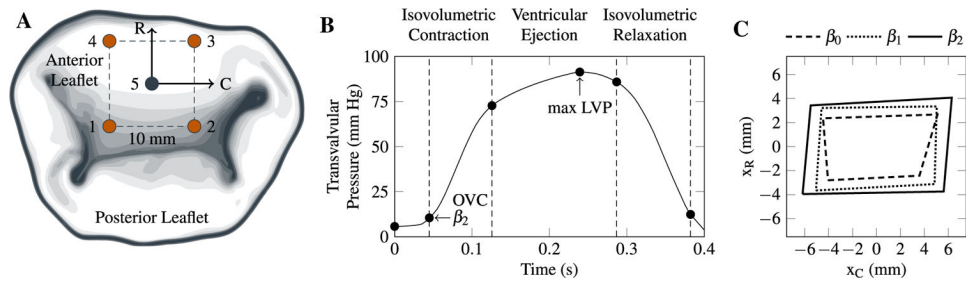
Fig. 1.
a Schematic of the mitral valve leaflet anterior leaflet along with the placement of the four/five sonocrystal transducers on the clear zone of the anterior leaflet. **b** Representation of the measured transvalvular pressure over one cardiac cycle. OVC: onset of ventricular contraction, represents the in vivo reference configuration β_2. Max LVP: Maximum left ventricular pressure, represents the maximum pressure-loaded state. **c** Illustration of the effects of in vivo pre-stress, highlighting the importance of considering β_2 instead of β_0 as the reference configuration
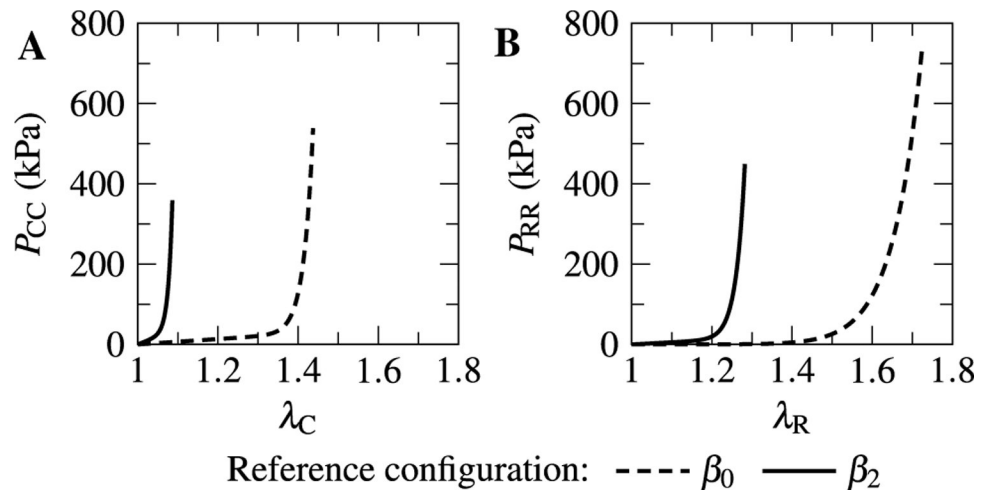
Fig. 2.
Illustration of referential configuration effects on the **a** circumferential and **b** radial stress–strain curves for the MVAL. Use of the in-vivo reference configuration β_2 results eliminates most of the low stiffness toe region and reduces overall strain levels
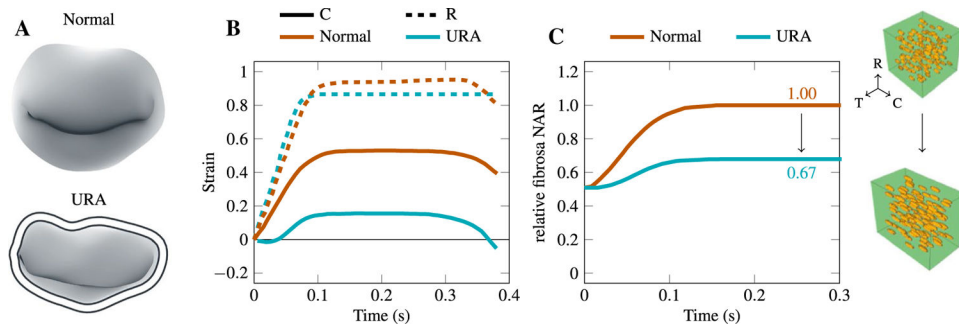
Fig. 3.

Illustration of simulation-driven experimental study. **a** Illustration of normal and repaired MV as the two primary states of interest. **b** Simulations of the model developed by Lee et al. (2017) suggest that the circumferential strains are dramatically altered after URA, whereas the radial strains remain unchanged. **c** Simulations from Lee et al. (2017) also suggest that the fibrosa NAR decreases by one-third following URA
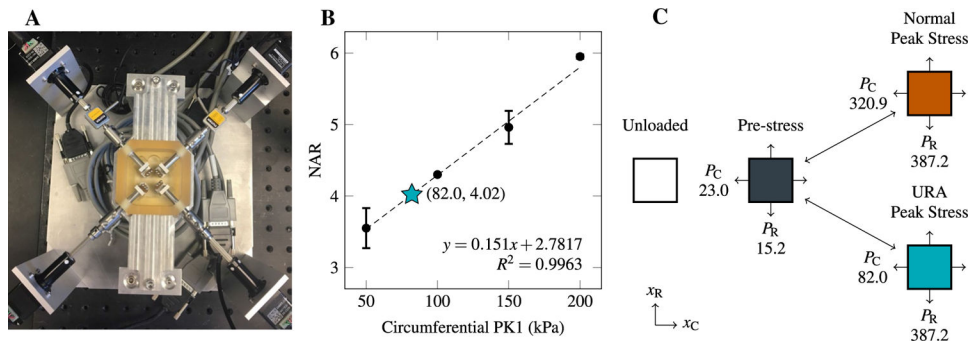
Fig. 4.
Illustration of the in vivo-mimicking PBBS experiments conducted herein. **a** Visualization of the PBBS. **b** MVIC NAR as a function of P_{CC}) and constant $P_{RR} = 387.2$ kPa. Linear regression is used to compute the P_{CC} that results in the desired URA NAR (teal star). **c** Illustration of the stress configurations used in the PBBS. Samples were either fixed in a single configuration or cycled between pre-stress and either normal peak stress or URA peak stress. All stresses are given in units of kPa
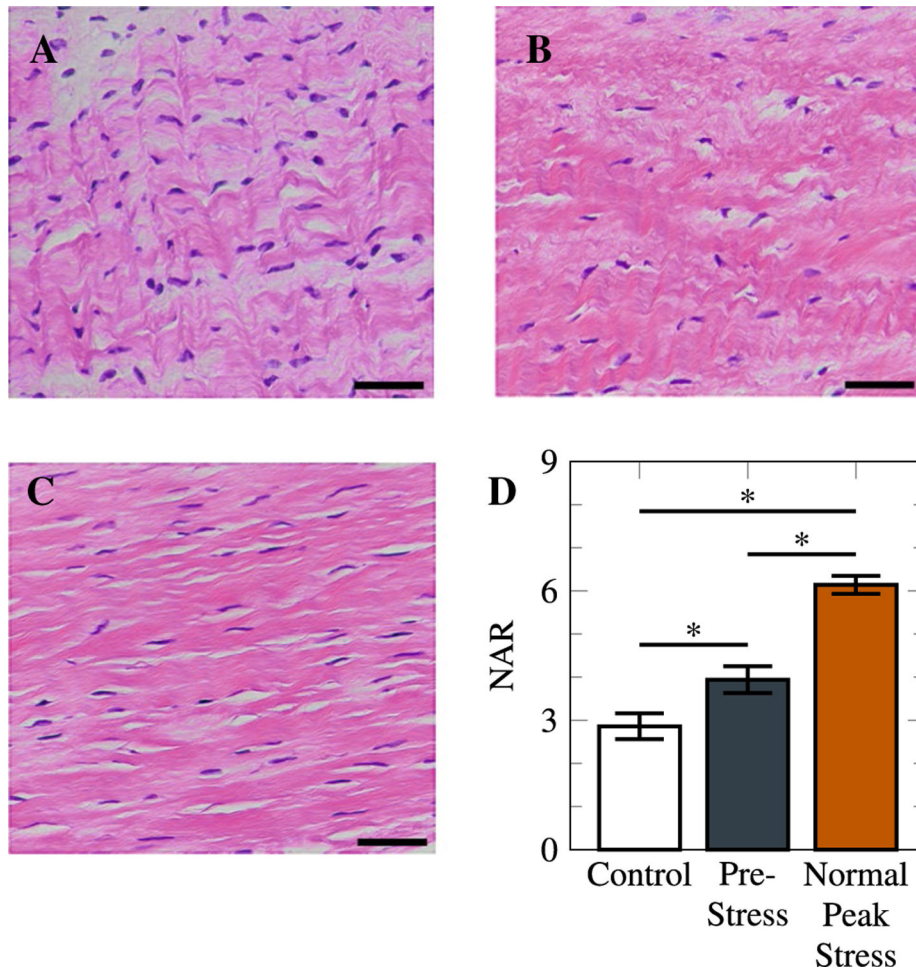
Fig. 5.
MVIC deformation quantified by the NAR. Representative H&E images from **a** a control sample, **b** a sample fixed under pre-stress, and **c** a sample fixed under normal stress with MVIC nuclei are stained in purple (Scale bar: 100 μm). **d** MVIC NAR was measured for n = 10 cells/sample for n = 3 samples/leaflets. Asterisks (*) indicate statistical significance by two-sample t test with $p < 0.01$
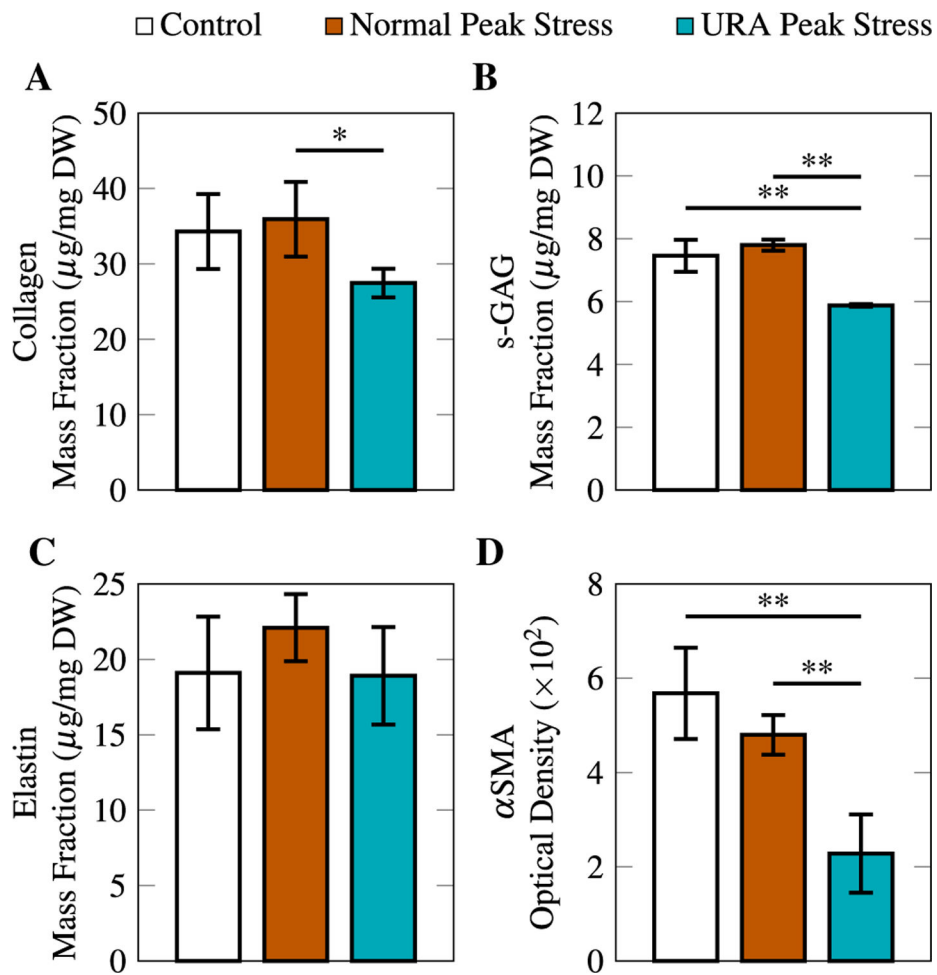
Fig. 6.
Effects of URA peak stress on ECM composition and VIC activation. Mass fractions of **a** collagen **b** s-GAG **c** elastin, as well as **d** α-SMA levels after 48 h cycling between pre-stress and either normal peak stress or URA peak stress, compared with postmortem controls. All bar graphs represent mean ± SEM, $n = 3$. Asterisks (*) and (**) indicate statistical significance by a one-tail, two-sample t test with $p < 0.1$ and $p < 0.05$, respectively
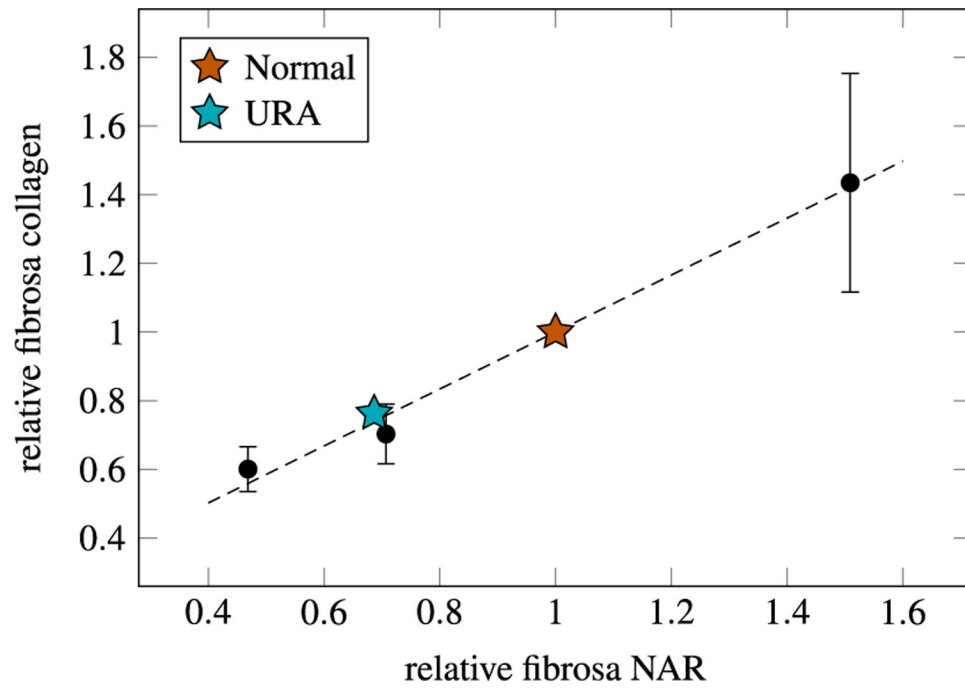
Fig. 7.
Relative change in VIC NAR predicts ECM collagen mass fraction. Previous results from (Ayoub et al. 2017) are used to predict the difference between cycling from pre-stress to normal peak stress (orange star) and cycling from pre-stress to URA peak stress (teal star) for 48 h in this study

Table 1

Difference in NAR between normal and URA groups parallels changes in tissue collagen and s-GAG. Predicted decreases come from comparison with Ayoub et al. (2017)

	Normal	URA	Observed % Decrease	Predicted % Decrease
NAR	6.03	4.14	31.3	33.3
Collagen	35.93	27.47	23.5	26.0
s-GAG	7.80	5.88	24.6	18.2